photonics

MDPI

Article

Design and Co-Simulation of an Integrated Thin-Film Lithium Niobate Optical Frequency Comb for SDM Interconnects

Haichen Wang [1,2], Jiahao Si [1,2], Jingxuan Chen [1], Zhaozheng Yi [1,2], Shuyuan Shi [3], Mingjin Wang [1,2,4,5,*] and Wanhua Zheng [1,2,4,5,*]

[1] Laboratory of Solid State Optoelectronics Information Technology, Institute of Semiconductors, Chinese Academy of Sciences, Beijing 100083, China; wanghaichen@semi.ac.cn (H.W.)
[2] Center of Materials Science and Optoelectronics Engineering, University of Chinese Academy of Sciences, Beijing 100049, China
[3] MIIT Key Laboratory of Spintronics, Fert Beijing Institute, School of Integrated Circuit Science and Engineering, Beihang University, Beijing 100191, China
[4] College of Future Technology, University of Chinese Academy of Sciences, Beijing 101408, China
[5] Hangzhou Institute for Advanced Study, University of Chinese Academy of Sciences, Hangzhou 310024, China
* Correspondence: mingjinwang@semi.ac.cn (M.W.); whzheng@semi.ac.cn (W.Z.)

Abstract

We propose a monolithically integrated optical frequency comb (OFC) generation platform on thin-film lithium niobate (TFLN), featuring cascaded dual-drive Mach–Zehnder modulators (DDMZM) and a Si_3N_4-assisted spot size converter (SSC). To capture microscopic mode mismatches and spatial phase accumulation often overlooked in idealized scalar simulations, we establish a multi-physics co-simulation framework integrating finite-difference time-domain (FDTD) analysis with macroscopic transmission modeling. Based on this framework, the cascaded modulator architecture generates 25 highly stable comb lines with a dense 2 GHz spacing and an envelope flatness within 2 dB. Tolerance analysis indicates that the comb generation is highly resilient to typical manufacturing and environmental variations, including thermal bias drift, RF phase mismatch, and half-wave voltage (V_π) dispersion. Furthermore, physical-layer modeling shows that the integrated SSC reduces fiber-to-chip coupling loss to 0.55 dB per facet, preserving the necessary optical power budget. To validate the platform's viability as a multi-wavelength continuous-wave source for spatial-division multiplexed (SDM) interconnects, a parallel transmission over a 20 km standard single-mode fiber is modeled. Using a digital signal processing (DSP)-free 10 Gb/s non-return-to-zero (NRZ) scheme, the 25-channel system maintains a worst-case bit error rate strictly below the forward error correction (FEC) threshold. This work offers a practical, physics-based evaluation framework for high-density co-packaged optics (CPO).

Keywords: electro-optic frequency comb; monolithic integration; thin-film lithium niobate; spot size converter

Check for updates

Received: 23 March 2026
Revised: 3 April 2026
Accepted: 8 April 2026
Published: 23 April 2026

Copyright: © 2026 by the authors. Licensee MDPI, Basel, Switzerland. This article is an open access article distributed under the terms and conditions of the Creative Commons Attribution (CC BY) license.

1. Introduction

The rapid growth of global data traffic, primarily driven by cloud computing, artificial intelligence clusters, and high-definition streaming, continues to push optical interconnects toward their capacity limits [1]. To address the evolving requirements for power efficiency, low latency, and bandwidth density in data centers, architectures such as CPO and SDM

have become highly relevant. In these architectures, OFCs can serve as compact, multi-wavelength continuous-wave (CW) sources for parallel transceiver arrays, offering distinct advantages in frequency stability and footprint [2,3].

TFLN has drawn considerable attention for integrated photonics due to its large electro-optic coefficient ($r_{33} \approx 30$ pm/V), low propagation loss, and strong optical confinement [4]. Recent developments in TFLN-based modulators [5] and fiber-to-chip interfaces [6] highlight the platform's potential for large-scale integration.

Despite these advances, modeling monolithically integrated TFLN OFC systems remains challenging. First, generating a flat frequency comb via electro-optic modulation requires complex architectures, such as cascaded modulators [7], which rely on multi-stage nonlinear phase modulation to overcome the poor spectral flatness typical of single-modulator approaches [8]. The performance of these cascaded structures is often sensitive to fabrication imperfections and environmental changes—such as V_π dispersion and thermo-optic bias drift [9,10]—which are frequently simplified or neglected in system-level simulations.

Second, the significant mode field mismatch between standard single-mode fibers (MFD $\approx$ 10.4 μm) and TFLN ridge waveguides (MFD $\approx$ 1–2 μm) introduces substantial coupling losses. While Si_3N_4-assisted SSCs [11,12] are commonly used to mitigate this, typical system-level link models treat these components as static scalar attenuators [13,14]. Such idealization fails to capture the wavelength-dependent microscopic mode overlap and the distributed phase evolution along the adiabatic tapers, leading to overestimations of the system's signal-to-noise ratio (SNR).

In this paper, we present a complete OFC architecture that unifies cascaded DDMZMs with an inverse-taper SSC on a TFLN platform. We evaluate this design using a customized FDTD-MATLAB 2021-OptiSystem co-simulation framework that directly incorporates electromagnetic-extracted transfer matrices into the link evaluation. This approach bridges the gap between physical design and system evaluation. We first present the OFC generation and its tolerance to practical physical deviations. Subsequently, we detail the SSC mode evolution and demonstrate how the recovered power budget enables a 25-channel, 10 Gb/s parallel SDM transmission over 20 km without the need for complex DSP.

2. Cascaded Ddmzm Architecture and Tolerance Analysis

2.1. System Topology and Comb Generation

To provide a compact, multi-wavelength optical source for high-density interconnects, we designed a cascaded DDMZM OFC architecture. As illustrated in Figure 1, the CW optical signal propagates through the primary DDMZM (DDMZM 1), driven by a 10 GHz RF signal, which defines the wide primary comb lines. The optical field then enters the secondary DDMZM (DDMZM 2), driven by a 2 GHz RF signal. This secondary stage populates the dense sub-comb lines through cascaded nonlinear phase modulation. A dense 2 GHz spacing is particularly advantageous for short-reach SDM: it allows spatial demultiplexing into parallel arrays while confining the 25-line comb to a narrow absolute bandwidth (~50 GHz), thereby minimizing material group velocity dispersion (GVD) penalties.

In such a cascaded setup, the DC bias voltage of the final-stage modulator is critical for determining spectral flatness. We apply an asymmetric bias scheme to shift the power distribution between the central carrier and its sidebands, which suppresses central carrier protrusion. The RF drive frequencies of 10 GHz DDMZM1 and 2 GHz DDMZM2 are chosen to satisfy two simultaneous constraints: the 2 GHz comb spacing confines 25 lines within a ~50 GHz absolute bandwidth, minimizing GVD penalties over 20 km SSMF; and the 5:1 frequency ratio between the two stages enables efficient sub-comb line population without harmonic aliasing between stages. The DDMZM2 bias of 1.225 V was obtained

by sweeping the DC bias across the [0, V_π] range and selecting the value that minimizes peak-to-peak power variation across the 25 comb lines. The DDMZM1 bias of 2 V (=$V_\pi/2$) places the modulator at the quadrature point to maximize linear sideband generation. The push-pull (180° phase) drive configuration for both modulators suppresses even-order harmonics and maintains spectral symmetry. A narrow-linewidth (100 kHz) external-cavity laser (ECL) is selected as the pump source to minimize phase noise transfer to the generated comb lines. Assuming a standard TFLN half-wave voltage (V_π = 4 V) and an input CW laser with a 100 kHz linewidth at 193.1 THz, we optimized the DDMZM 2 bias voltage to 1.225 V. The comprehensive physical parameter configuration of the system, taking into account typical component specifications, is detailed in Table 1.

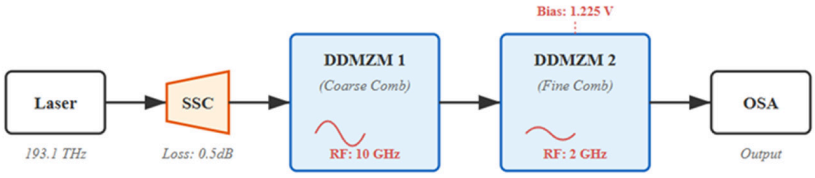


Figure 1. Architecture of the optical frequency comb generation system based on cascaded DDMZMs.

Table 1. Cascaded DDMZM key parameter configuration.

Device	Parameter	Value	Physical Significance
CW Laser	Center Frequency	193.1 THz	C-band standard reference
	Linewidth	100 kHz	Narrow-linewidth external-cavity laser (ECL)
DDMZM1	V_π	4 V	Typical TFLN modulator value
	DC Bias	2 V	Maximize sidebands in linear region
	RF Frequency/Phase	10 GHz/180°	Push-pull drive mode
DDMZM2	V_π	4 V	-
	DC Bias	1.225 V	Asymmetric bias for flatness optimization
	RF Frequency/Phase	2 GHz/180°	Generate dense sub-comb lines

Figure 2 shows the resulting OFC spectrum based on these parameters. The 25 distinct comb lines are uniformly separated by the 2 GHz drive frequency. The spectral envelope's power fluctuation is maintained within 2 dB, and the side-mode suppression ratio exceeds 40 dB, meeting the light source uniformity requirements for multi-channel communication [15].

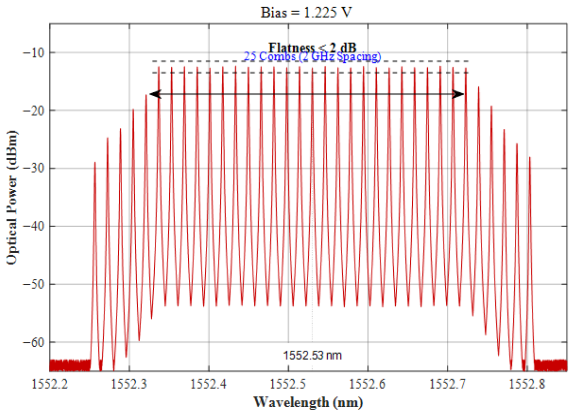


Figure 2. Output spectrum of the 25-line optical frequency comb, showing a spectral envelope fluctuation within 2 dB.

2.2. Tolerance Analysis Against Physical Imperfections

Practical device performance often deviates from ideal simulation targets due to environmental variations and fabrication tolerances. We evaluated the robustness of the proposed OFC under three primary sources of perturbation: thermal bias drift, RF phase mismatch, and V_π variation. The consolidated results are presented in Figure 3.

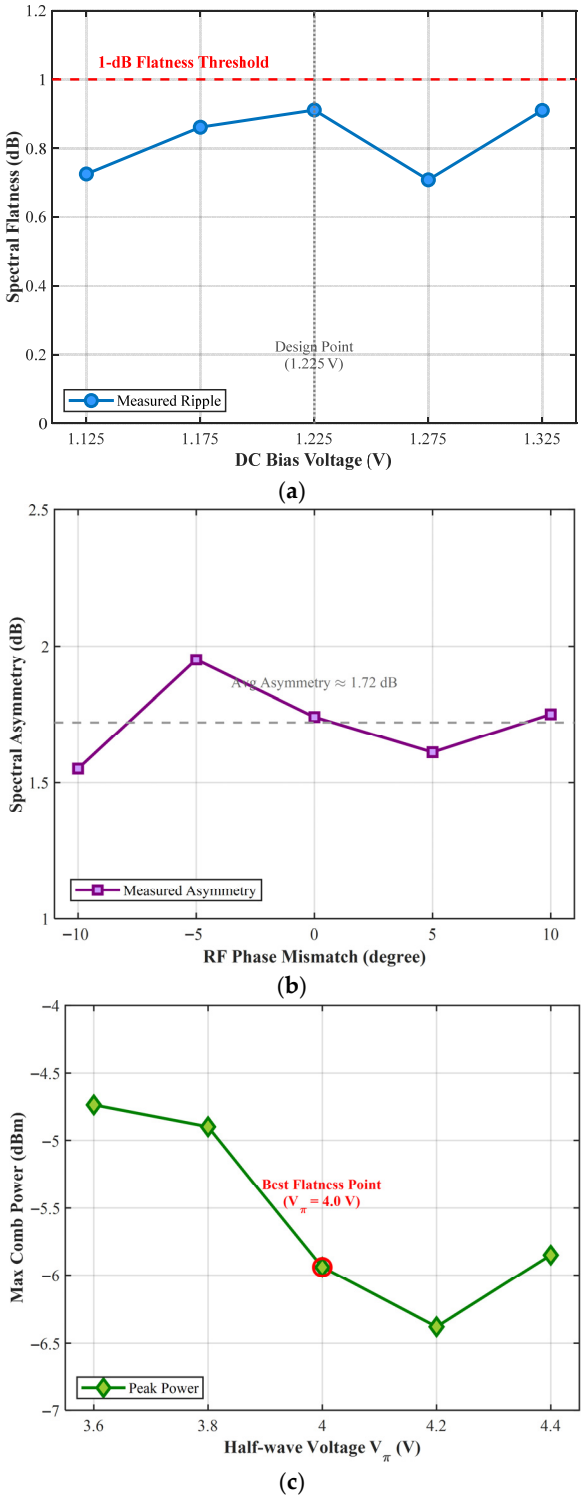


Figure 3. Tolerance analysis of the OFC generation. (**a**) Impact of DDMZM 2 DC bias voltage drift on spectral flatness. (**b**) Effect of RF drive signal phase mismatch on spectral symmetry. (**c**) Peak power fluctuation induced by TFLN V_π variations, where "peak power fluctuation" denotes the maximum power variation among individual comb lines across the 25-line spectrum.

Thermal Robustness (Figure 3a): Ambient temperature fluctuations modify the waveguide's effective refractive index (n_{eff}) via the thermo-optic effect, causing DC bias drift. We varied the second-stage DC bias from 1.125 V to 1.325 V ($\pm$0.1 V), corresponding to typical thermal drifts [16]. The spectral flatness remains below 1 dB (peaking at 0.911 dB) within this range, indicating that stringent, sub-Kelvin thermal stabilization is not necessary for this architecture [17].

RF Phase Mismatch (Figure 3b): Lithographic variations in RF routing can cause slight phase deviations from the ideal 180° anti-phase push-pull state. Under simulated phase errors up to $\pm 10°$, the spectral asymmetry remains bounded between 1.55 dB and 1.95 dB. This variation is sufficiently small to maintain uniform carrier powers for subsequent modulation.

V_π Process Variation (Figure 3c): Wafer-level etch depth and electrode gap variations lead to fluctuations in the modulator's half-wave voltage. Sweeping the V_π from 3.6 V to 4.4 V (a $\pm$10% margin) results in a global OFC peak power variation of only 1.6 dB. This minor power penalty can be readily managed by standard optical amplification prior to fiber launch.

3. Spot Size Converter Design and Co-Simulation

Although the OFC architecture exhibits strong tolerance to modulation imperfections, extracting the comb for practical link use requires efficient fiber-to-chip coupling. To physically model this interface, we implemented a Si_3N_4-assisted inverse taper SSC.

3.1. Mode Field Evolution and Coupling Modeling

The proposed Si_3N_4-assisted inverse taper SSC employs a highly optimized heterogeneous integration (Figure 4). The bottom SiO_2 substrate ($n \approx 1.46$) isolates the optical mode from the underlying silicon. The middle $LiNbO_3$ film (thickness $h_{LN} = 600$ nm, $n_e \approx 2.14$ at 1550 nm) serves as the primary waveguide core. The TFLN ridge waveguides are modeled assuming fabrication via electron-beam lithography (EBL) patterning, followed by inductively coupled plasma reactive-ion etching (ICP-RIE) of an X-cut $LiNbO_3$ thin film. A 200 nm unetched slab is strictly retained to mitigate sidewall scattering loss. Drawing upon state-of-the-art empirical data, a practical propagation loss of 0.3–1.0 dB/cm is assigned to the TFLN waveguides, ensuring that the total on-chip propagation loss contribution remains securely within the link power budget established in Section 4 [1].

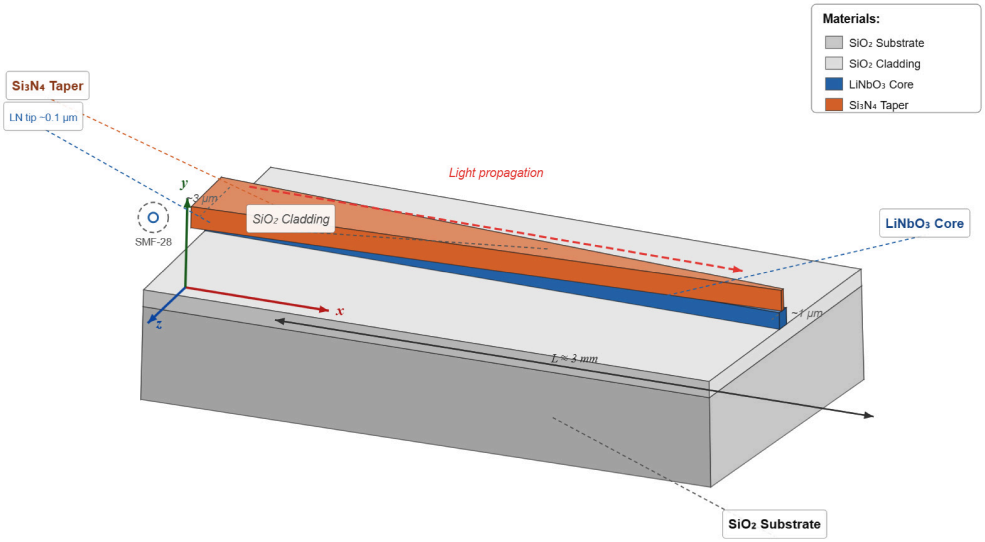


Figure 4. Three-dimensional schematic of the Si_3N_4-assisted inverse taper spot size converter on a TFLN platform.

To address mechanical stability and material compatibility, the top Si_3N_4 layer ($h_{SiN} = 1.2$ µm) is modeled via low-pressure chemical vapor deposition (LPCVD). Crucially, it is patterned into a discrete, narrow inverse taper strip rather than a continuous blanket film. This geometric confinement substantially relieves the massive intrinsic tensile stress (typically ≈ 1 GPa for stoichiometric LPCVD Si_3N_4), thereby preventing film cracking or delamination from the underlying TFLN. Furthermore, the SiO_2 interlayer strategically positioned between the Si_3N_4 and TFLN operates as a compliant mechanical buffer. This robust fabrication approach has been experimentally validated in prior designs, demonstrating exceptional structural integrity without delamination [12].

The Si_3N_4 inverse taper narrows adiabatically from $w_{in} = 10.0$ µm at the fiber facet to $w_{out} = 1.8$ µm over a total transition length $L = 3$ mm. This specific length is stringently designed to satisfy the adiabatic criterion. The local taper half-angle reaches a maximum of approximately 1.7 mrad, remaining well below the threshold dictated by the local effective index contrast between the fundamental and first higher-order modes, formulated as $\theta(z) \ll \left(n_{eff,1} - n_{eff,2}\right) / \left(2n_{eff,1}\right)$. Rigorous FDTD verification confirms that higher-order mode excitation is uniformly suppressed below −30 dB throughout the entire taper, validating authentic adiabatic mode evolution and negligible non-adiabatic power leakage.

FDTD simulations track the mode field evolution (Figure 5). At the fiber facet ($w = 10.0$ µm), the mode profile roughly matches a standard SMF-28 fiber. Through the adiabatic transition region, the mode compresses downwards, eventually confining tightly within the $LiNbO_3$ waveguide (MFD ≈ 1.1 µm) at the chip facet without exciting higher-order modes.

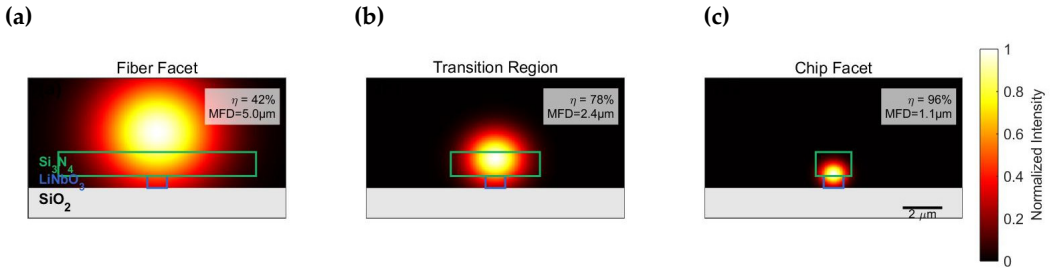


Figure 5. Optical mode field evolution. (**a**) SMF-matched mode at the fiber facet. (**b**) Adiabatic transition region. (**c**) Tightly confined mode at the chip facet.

3.2. Multi-Physics Joint Simulation Framework

To evaluate the impact of this coupling interface on the overall communication link, we bypassed standard scalar loss approximations by establishing a three-stage FDTD-MATLAB-OptiSystem co-simulation framework (Figure 6).

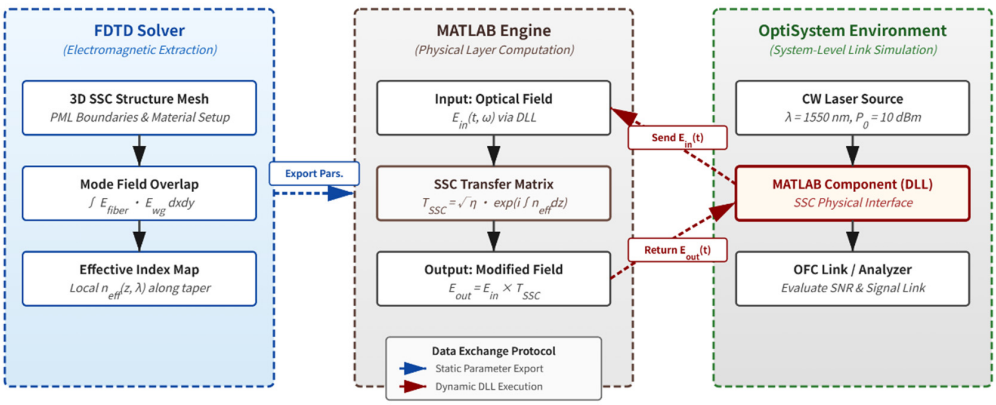


Figure 6. Schematic diagram of the multi-physics joint simulation data flow integrating FDTD, MATLAB, and OptiSystem.

Initially, the FDTD electromagnetic solver explicitly computes the spatially dependent parameters of the 3D waveguide physical design, extracting the local effective refractive index $n_{\text{eff}}(z)$ and the electromagnetic mode overlap integral ($\int E_{\text{fiber}} \cdot E_{\text{wg}}$). These raw physical parameters are exported to the MATLAB engine, which performs a rigorous path-integral computation to generate a complex, wavelength-dependent transfer matrix (T_{SSC}). Finally, OptiSystem passes the dynamic optical field $E_{\text{in}}(t)$ via a dynamic link library (DLL) interface to MATLAB, where the exact physical degradation and phase accumulation are applied before returning the modified field $E_{\text{out}}(t)$ to the system link. This ensures that localized spatial mode mismatches and exact phase evolution are authentically reflected in the macroscopic communication simulation [18].

Simulation of the isolated SSC confirms a broadband minimum insertion loss of 0.55 dB at 1550 nm, with 1 dB alignment penalties at approximately ±1.49 µm (horizontal) and ±1.08 µm (vertical) (Figure 7), which is well within standard active alignment capabilities.

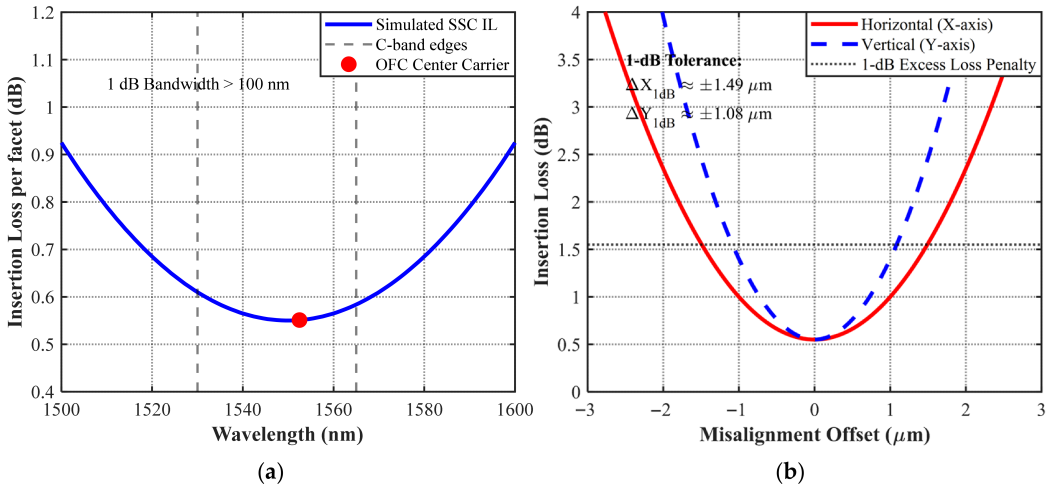


Figure 7. (**a**) Wavelength-dependent insertion loss of the SSC. (**b**) Alignment tolerance profile.

When incorporated into the full comb-generation link, the integration of the SSC significantly improves the power budget. As shown in Figure 8, a direct facet coupling scheme suffers a massive 9.56 dB penalty relative to the ideal limit, dropping peak carrier power to −22.25 dBm. By utilizing the SSC, the peak power is restored to −12.84 dBm, effectively retrieving approximately 9.4 dB of the optical power.

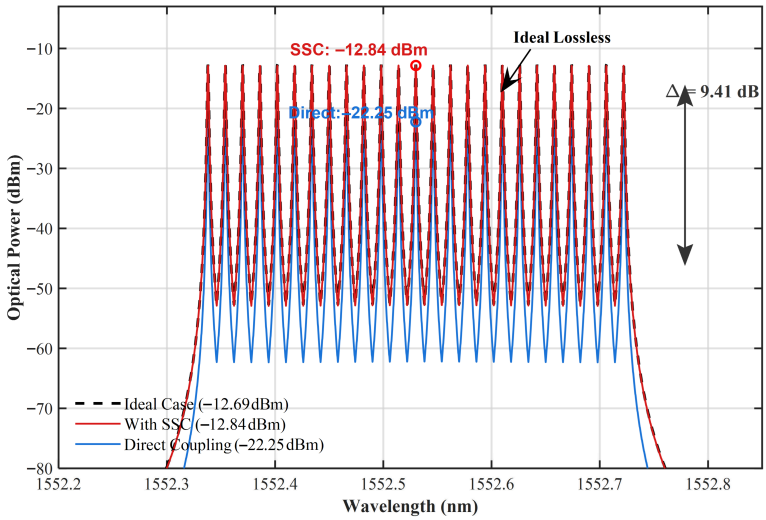


Figure 8. Comparison of OFC spectral power using direct coupling versus the proposed SSC integration.

The specific link power variations under different coupling scenarios are quantitatively summarized in Table 2. This power recovery is essential to maintain the necessary SNR for subsequent fiber transmission [19].

Table 2. Link power loss comparison under different coupling schemes.

Coupling Scheme	Peak Power (dBm)	Relative Loss (dB)	Evaluation
Ideal (Reference)	−12.69	0 (Ref.)	Theoretical limit
SSC Integration (This Work)	−12.84	0.15	Near-ideal, minimal loss
Direct Coupling	−22.25	9.56	Excessive loss, impractical

4. System-Level Transmission Validation

To empirically verify the data-carrying capability of the generated optical comb in short-reach interconnect scenarios, we modeled a complete parallel SDM optical transmission link (Figure 9). The system avoids advanced DSP to isolate and evaluate the fundamental optical integrity of the carriers, utilizing a straightforward baseband NRZ modulation format.

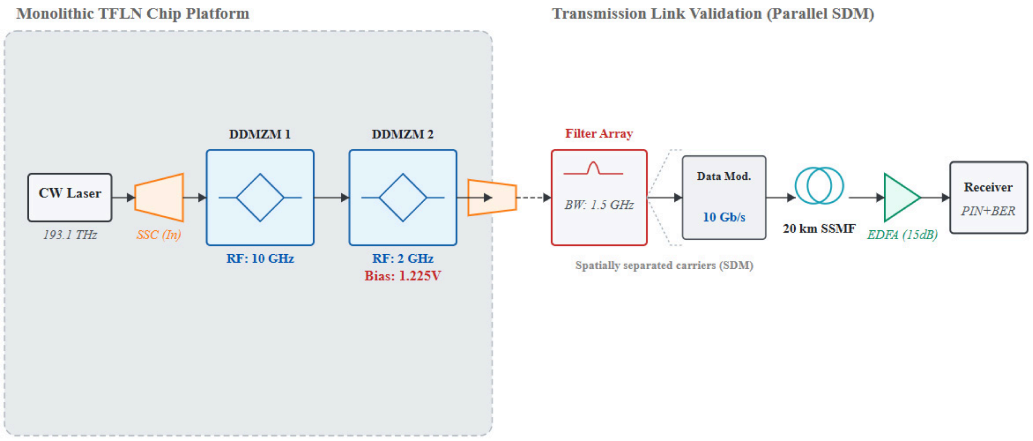


Figure 9. Simulation setup for the parallel SDM optical transmission system using the integrated TFLN OFC as the multi-wavelength source.

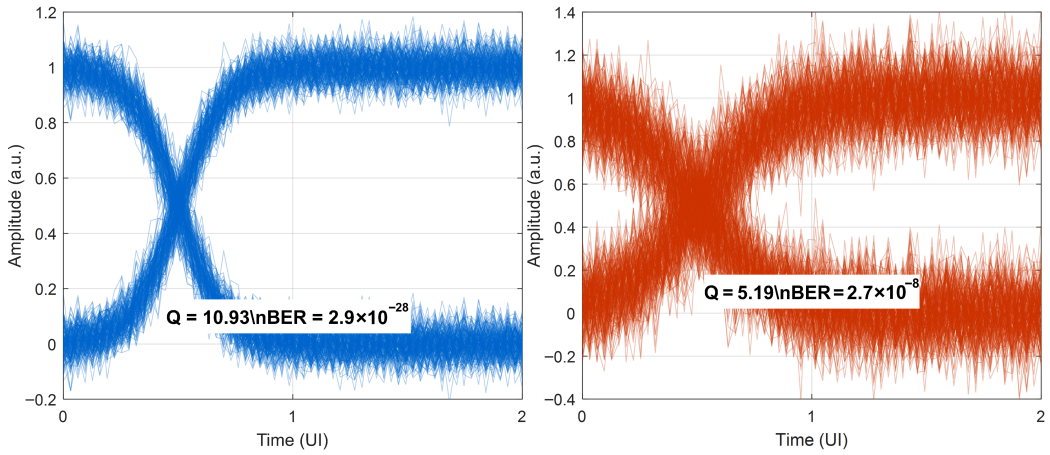
The transmission link operates through three primary stages. At the transmitter side, the 25 generated comb lines are separated using an array of optical bandpass filters with a 1.5 GHz passband. Each isolated CW carrier is routed to an independent spatial channel, where a discrete lithium niobate Mach–Zehnder modulator encodes a 10 Gb/s NRZ pseudo-random binary sequence (PRBS, length $2^{10} - 1$).

During propagation, the modulated optical signals are launched into a 20 km standard single-mode fiber (SSMF) array. The signal evolution in the fiber is modeled via the nonlinear Schrödinger equation, accounting for standard fiber characteristics including a 0.2 dB/km attenuation, 16.75 ps/(nm·km) chromatic dispersion, and Kerr nonlinearity. To offset accumulated link and insertion losses, an erbium-doped fiber amplifier (EDFA) array providing 15 dB of gain is placed at the receiver front-end.

At the receiver, direct detection is performed using a PIN photodiode array with a responsivity of 1 A/W. The recovered electrical signals are low-pass filtered (Bessel filter, 7.5 GHz cutoff) and fed into an error analyzer to evaluate the eye diagrams and calculate the system Q-factors and bit error rates (BER). We evaluated the signal quality across the spectrum, specifically analyzing the central carrier (193.100 THz) and a marginal carrier at the comb's edge (193.110 THz).

The received signal for the central carrier (Figure 10a) displays a wide eye opening and clean crossing points. Given its position at the spectral peak, this channel enjoys the

highest initial optical SNR, resulting in a system Q-factor of 10.93 and a baseline BER of 2.92×10^{-28}.



(**a**) (**b**)

Figure 10. Received eye diagrams after 20 km SDM transmission. (**a**) The central carrier (193.100 THz). (**b**) A marginal edge carrier (193.110 THz).

Conversely, the edge carrier (Figure 10b) exhibits slight time-domain degradation, primarily due to the natural power roll-off at the comb edges (which increases susceptibility to spontaneous emission noise post-amplification) and accumulated fiber dispersion. Despite these factors, the eye remains open, yielding a deterministic Q-factor of 5.19 and a BER of 2.72×10^{-8}.

To quantitatively verify the commercial viability of all spatially multiplexed comb lines, the deterministic transmission performance data for the key spatial channels are summarized in Table 3.

Table 3. Multi-carrier SDM transmission performance evaluation.

Channel Type	Frequency (THz)	Q-Factor	Min BER	Evaluation
Center Carrier	193.100	10.93	2.92×10^{-28}	Excellent (No FEC needed)
Middle Carrier	193.110	5.19	2.72×10^{-8}	Qualified (FEC correctable)
Edge Carrier	193.124	>4.5	$< 1 \times 10^{-5}$	Qualified (FEC correctable)

As shown, even for the most degraded edge channel (BER $< 1 \times 10^{-5}$), the error rate remains comfortably below the standard ITU-T G.975 FEC threshold of 3.8×10^{-3}. This confirms that all 25 comb lines can function as independent, reliable communication channels, yielding an aggregate parallel capacity of 250 Gb/s (25 × 10 Gb/s) and validating the integrated platform for next-generation short-reach optical interconnects [20].

5. Discussion

While this joint-simulation framework provides a more realistic assessment than purely ideal models by incorporating spatial phase tracking and manufacturing tolerances, numerical boundaries remain. The model assumes adequate RF isolation between the closely spaced DDMZMs. In physical deployment, the dense RF routing for the 2 GHz and 10 GHz signals could introduce electromagnetic crosstalk, necessitating careful electrode spacing and grounding design. Additionally, while the parallel SDM setup avoids four-wave mixing (FWM) crosstalk typical of WDM systems, the current co-simulation utilizes an ideal CW pump laser. Future experimental work will be needed to fully characterize the impact of practical diode laser phase noise and relative intensity noise (RIN) within this integrated platform.

From a fabrication perspective, the proposed platform is compatible with existing TFLN foundry processes. The TFLN ridge waveguides can be patterned by EBL or DUV lithography followed by ICP-RIE etching, with demonstrated propagation losses below 1 dB/cm in multi-project wafer runs [1]. The Si_3N_4 SSC layer can be deposited by LPCVD and patterned separately prior to integration on the TFLN substrate, following the process validated in [12]. Key fabrication challenges include controlling TFLN etch depth uniformity across the wafer—which directly affects V_π—managing Si_3N_4 film stress through taper geometry as described in Section 3.1, and achieving precise RF electrode alignment for the DDMZMs. On-chip resistive heaters can be integrated to compensate for thermo-optic bias drift; the tolerance analysis in Section 2.2 confirms that sub-Kelvin thermal stabilization is not required. Full experimental validation of the integrated platform is planned as future work.

6. Conclusions

We presented the design and co-simulation of a monolithically integrated OFC platform on TFLN, evaluated using a customized FDTD-MATLAB-OptiSystem multi-physics framework. The central methodological contribution of this work is the direct embedding of FDTD-extracted electromagnetic transfer matrices into the system-level link model, replacing idealized scalar approximations with spatially resolved mode overlap and phase evolution. This approach demonstrated that the Si_3N_4-assisted SSC nearly eliminates the coupling penalty of direct fiber-to-chip interfaces, and that the cascaded DDMZM architecture is robust against practical manufacturing and environmental deviations. System-level validation confirms that the 25-line comb supports DSP-free parallel SDM transmission within standard FEC limits. This physics-based co-simulation methodology is broadly applicable to the rigorous evaluation of integrated photonic platforms for scalable, high-density co-packaged optical links.

Author Contributions: Conceptualization, H.W.; Methodology, H.W., J.S. and Z.Y.; Software, H.W., J.S. and Z.Y.; Validation, H.W.; Formal analysis, H.W.; Data curation, H.W.; Writing—original draft, H.W.; Writing—review & editing, J.C.; Supervision, M.W. and W.Z.; Project administration, M.W. and W.Z.; Funding acquisition, S.S., M.W. and W.Z. All authors have read and agreed to the published version of the manuscript.

Funding: This work was supported by National Natural Science Foundation of China (62205328), Beijing Nova Program (20230484332, 20240484654).

Data Availability Statement: Data underlying the results presented in this paper are not publicly available at this time but may be obtained from the authors upon reasonable request.

Conflicts of Interest: The authors declare no conflicts of interest.

References

1. Zhu, D.; Shao, L.; Yu, M.; Cheng, R.; Desiatov, B.; Xin, C.J.; Hu, Y.; Holzgrafe, J.; Ghosh, S.; Shams-Ansari, A.; et al. Integrated photonics on thin-film lithium niobate. *Adv. Opt. Photonics* **2021**, *13*, 242–352. [CrossRef]
2. Gaeta, A.L.; Lipson, M.; Kippenberg, T.J. Photonic-chip-based frequency combs. *Nat. Photonics* **2019**, *13*, 158–169. [CrossRef]
3. Wang, C.; Zhang, M.; Chen, X.; Bertrand, M.; Shams-Ansari, A.; Chandrasekhar, S.; Winzer, P.; Lončar, M. Integrated lithium niobate electro-optic modulators operating at CMOS-compatible voltages. *Nature* **2018**, *562*, 101–104. [CrossRef]
4. Zhang, M.; Buscaino, B.; Wang, C.; Shams-Ansari, A.; Reimer, C.; Zhu, R.; Kahn, J.M.; Lončar, M. Broadband electro-optic frequency comb generation in a lithium niobate microring resonator. *Nature* **2019**, *568*, 373–377. [CrossRef]
5. Xu, M.; He, M.; Zhang, H.; Jian, J.; Pan, Y.; Liu, X.; Chen, L.; Meng, X.; Chen, X.; Li, Z.; et al. High-performance coherent optical modulators based on thin-film lithium niobate platform. *Nat. Commun.* **2020**, *11*, 3911. [CrossRef]
6. He, L.; Zhang, M.; Shams-Ansari, A.; Zhu, R.; Wang, C.; Lončar, M. Low-loss fiber-to-chip interface for lithium niobate photonic integrated circuits. *Opt. Lett.* **2019**, *44*, 2314–2317. [CrossRef]

7. Wu, X.; Cheng, C.; Fu, J.; Liu, M. Generation of flat electro-optic frequency combs based on cascaded modulators. *J. Light. Technol.* **2020**, *38*, 5100–5106.
8. Liu, J.; Huang, G.; Wang, R.N.; He, J.; Raja, A.S.; Liu, T.; Engelsen, N.J.; Kippenberg, T.J. High-yield wafer-scale fabrication of ultralow-loss, dispersion-engineered silicon nitride photonic circuits. *Nat. Commun.* **2021**, *12*, 2236. [CrossRef]
9. He, M.; Xu, M.; Ren, Y.; Jian, J.; Ruan, Z.; Xu, Y.; Gao, S.; Sun, S.; Wen, X.; Zhou, L.; et al. High-performance hybrid silicon and lithium niobate Mach–Zehnder modulators for 100 Gbit/s and beyond. *Nat. Photonics* **2019**, *13*, 359–364. [CrossRef]
10. Gao, R.; Zhang, H.; Bo, F.; Fang, J.; Fang, K.; Wang, J.; Zhu, N.; Xiao, T.; Zhang, G. Broadband highly efficient nonlinear optical processes in on-chip integrated lithium niobate microdisk resonators of Q-factor above 10^8. *New J. Phys.* **2021**, *23*, 123027. [CrossRef]
11. Tian, Y.; Shao, L.; Zhang, M.; Zhu, R.; Reimer, C.; Wang, C.; Lončar, M. Adiabatic coupler for lithium niobate photonic integrated circuits. *Opt. Express* **2019**, *27*, 9794–9802.
12. Yi, Z.; Wang, M.; Liu, W.; Zhou, S.; Si, J.; Tang, C.; Xin, D.; Zheng, W. Integrated low-cost and low-loss spot size converter for thin film lithium niobate. *Opt. Express* **2023**, *31*, 8320–8329. [CrossRef]
13. Hu, Y.; Yu, M.; Zhu, D.; Sinclair, N.; Shams-Ansari, A.; Shao, L.; Holzgrafe, J.; Puma, E.; Zhang, M.; Lončar, M. On-chip electro-optic frequency shifters and beam splitters. *Nature* **2021**, *599*, 587–593. [CrossRef] [PubMed]
14. Shams-Ansari, A.; Yu, M.; Chen, Z.; Reimer, C.; Zhang, M.; Picqué, N.; Lončar, M. Thin-film lithium-niobate electro-optic platform for spectrally tailored dual-comb spectroscopy. *Commun. Phys.* **2022**, *5*, 88. [CrossRef]
15. Puttnam, B.J.; Rademacher, G.; Luís, R.S. Space-division multiplexing for optical fiber communications. *Optica* **2021**, *8*, 1186–1203. [CrossRef]
16. Chen, X.; Antonelli, C.; Chandrasekhar, S.; Raybon, G.; Sinsky, J.; Ryf, R. High-speed transmission systems using integrated lithium niobate modulators. *J. Light. Technol.* **2022**, *40*, 1610–1621.
17. Chen, Z.; Yu, M.; Lončar, M. Thin-film lithium niobate quantum photonics. *Laser Photonics Rev.* **2022**, *16*, 2200083. [CrossRef]
18. Fang, J.; Gao, R.; Wang, J.; Zhang, G. High-Q microresonators on a thin-film lithium niobate platform: A review. *J. Opt.* **2022**, *24*, 083002.
19. Agrawal, G.P. *Nonlinear Fiber Optics*, 6th ed.; Academic Press: Cambridge, MA, USA, 2019.
20. Kumar, M.K.S.; Erkilinc, S. Recent advances in direct detection systems for short-reach optical interconnects. *J. Opt. Commun. Netw.* **2021**, *13*, E41–E55. [CrossRef]

Disclaimer/Publisher's Note: The statements, opinions and data contained in all publications are solely those of the individual author(s) and contributor(s) and not of MDPI and/or the editor(s). MDPI and/or the editor(s) disclaim responsibility for any injury to people or property resulting from any ideas, methods, instructions or products referred to in the content.